Rare Metals

WILEY | 有科出版 YOUKE PUBLISHING

ORIGINAL ARTICLE OPEN ACCESS

Redox Reaction and Dissolution Analysis for Hollow *C* Nanospheres Comprising *N*-Doped *C* Framework With Abundant Ni–Co Heteronuclear Catalysts for Highly Durable K–Te Batteries

Sung Woo Cho[1] | Kun Woo Baek[1] | Thillai Govindaraja Senthamaraikannan[2] | Hyun Woo Kim[3] | Dong-Hee Lim[2] | Jin-Sung Park[4] | Rakesh Saroha[1,4] | Jung Sang Cho[1,5,6]

[1]Department of Engineering Chemistry, Chungbuk National University, Chungbuk, Republic of Korea | [2]Department of Environmental Engineering, Chungbuk National University, Chungbuk, Republic of Korea | [3]Department of Chemical Engineering, Gyeongsang National University, Jinju, Republic of Korea | [4]Department of Materials Science and Engineering, Ajou University, Suwon-si, Gyeonggi-do, Republic of Korea | [5]Biomedical Research Institute, Chungbuk National University Hospital, Chungbuk, Republic of Korea | [6]Advanced Energy Research Institute, Chungbuk National University, Chungbuk, Republic of Korea

Correspondence: Rakesh Saroha (rakeshsaroha.18787@gmail.com) | Jung Sang Cho (jscho@cbnu.ac.kr)

Received: 28 October 2025 | **Revised:** 15 December 2025 | **Accepted:** 19 December 2025

Keywords: density functional theory | double atom catalyst | exceptional potassium storage | polytelluride dissolution | porous carbon nanosphere

ABSTRACT

Tellurium (Te), emerging as a promising alternative to sulfur (S) and selenium (Se), offers significant advantages for potassium (K) ion storage due to its comparable theoretical volumetric capacity (2619 mAh cm^{-3}) and higher electronic conductivity (~10^2 S m^{-1}), which promotes rapid charge transfer and improves reaction kinetics. However, substantial volume changes during potassiation/depotassiation and the shuttling effect of polytellurides hinder the feasibility of K–Te batteries. Moreover, comprehensive studies on the phase formation and dissolution mechanism of K-polytellurides (K–pTe_n) employing various in situ and ex-situ techniques are scarcely reported. Herein, we introduce a rational strategy utilizing nickel (Ni) and cobalt (Co) heteronuclear double-atom catalysts (DACs) encapsulated within hollow porous carbon nanospheres (Ni/Co–N–HPCNS) as hosts for tellurium impregnation (Te–Ni/Co–N–HPCNS). In situ and ex-situ XRD analysis revealed continuous phase transformation during discharge from amorphous Te (starting at OCV) to K_2Te_3 (discharged to 1.5 V) and finally to K_5Te_3 (discharged to 0.5 V). During the reverse scan, K_5Te_3 was reversibly converted to K_2Te_3 (charged to 3.0 V). Additionally, density functional theory calculations have shown that the presence of Ni/Co–DAC significantly impedes the dissolution of K–pTe_n species, thereby expediting the reaction kinetics to unprecedented levels (3000 cycles at 2.0C). When tested as a negative electrode for K-ion storage in a full-cell layout, the prepared nanostructure exhibits highly reversible K-ion redox reactions, demonstrating its potential for commercial applications. We believe that the comprehensive design and characterization strategy discussed herein will open new frontiers for obtaining nanostructures with unparalleled electrochemical performances.

Sung Woo Cho and Kun Woo Baek have contributed equally to this study.

1 | Introduction

Currently, lithium–ion (Li-ion) batteries have become ubiquitous in various facets of human activity, from portable electronics to electric vehicles and large-scale power grids for energy storage systems [1, 2]. However, challenges including the scarcity and uneven distribution of raw materials (Li-precursors) in the Earth's crust, limited energy density (150–250 Wh kg^{-1}), and high production costs (~300–350 \$ kW^{-1} h^{-1}) are driving researchers globally to explore alternative reversible electrochemistry systems based on monovalent ions (Na^+ and K^+), divalent ions (Ca^{2+}, Mg^{2+}, and Zn^{2+}), and even the trivalent ion (Al^{3+}) [3–6]. Among monovalent ion-based redox systems, potassium–ion (K-ion) batteries (PIB) are notable, offering distinct advantages such as affordability due to their high abundance (1.5 wt% compared to 0.001 wt% for Li), high operational voltage, and high energy density, primarily derived from the comparable redox potential of the K/K^+ pair (−2.93 V vs. the standard hydrogen electrode (SHE)) to lithium (−3.04 V vs. SHE) and being slightly higher than sodium (−2.71 V vs. SHE) [7, 8]. The superior ionic conductivity and mobility of K-ions in electrolytes, attributed to their weak Lewis acid characteristics, result in a smaller Stokes radius (3.6 Å) compared to Na^+ (4.6 Å) and Li^+ (4.8 Å), giving them an edge over Li/Na-ion systems [8, 9]. However, challenges persist because of the larger ionic radii of K-ion (1.38 Å) compared with Li^+ (0.76 Å) and Na^+ (1.02 Å) [7, 10]. This discrepancy often results in sluggish redox kinetics and significant volume fluctuations during charge–discharge cycles, causing pulverization of electrode materials and subsequently degrading the electrochemical performance [11].

In recent years, there has been a notable shift toward utilizing group XVI chalcogen elements, specifically sulfur (S) and selenium (Se), as cathodes [12–14]. This transition is driven by their straightforward two-electron conversion-type redox chemistry, which contrasts with the intricacies associated with conventional intercalation cathodes [15–18]. Consequently, S-based (K_2S; 1675 mAh g^{-1}) and Se-based (K_2Se; 675 mAh g^{-1}) systems have demonstrated high theoretical discharge capacities [9, 19–22]. Despite these promising values, the low electronic conductivities of S (~10^{-28} S m^{-1}) and Se (~10^{-9} S m^{-1}) along with their discharge products, contribute to significant challenges. These include high active material loss related to the shuttle effect, which involves the migration of intermediate polysulfides or polyselenides toward the anode, and substantial volume perturbations, leading to poor rate capability and inferior cycling stabilities in K–S and K–Se batteries [23–25]. In contrast, semimetal tellurium (Te), also part of group XVI, displays higher electronic conductivity (~10^2 S m^{-1}), promoting rapid charge transfer characteristics and high active material utilization [1, 11]. Besides, Te has a high mass density of approximately 6.25 g cm^{-3}, yielding a notable gravimetric energy density (420 mAh g^{-1}) and a theoretical volumetric capacity (2619 mAh cm^{-3}) comparable to those of S (3467 mAh cm^{-3}) and Se (3275 mAh cm^{-3}) [26–28]. However, akin to S and Se-based cathodes, Te cathodes encounter significant challenges due to extensive volume changes (~400% for K_2Te) and the shuttle effect, which impede the practical application of K–Te batteries [7, 29].

To address these challenges, numerous techniques have been investigated, focusing primarily on developing nanostructures such as Te-embedded porous carbon nanofibers [7], microporous carbon/Te composites [30], and Te@nitrogen-doped carbon microspheres composites [31]. Additionally, strategies such as molecular-regulated Se–Te solid solutions [10], interfacial engineering [1], and glucose–carbon nanotube (G–CNT)/Te composites [11], have also been explored. Notably, prior studies have primarily focused on constructing porous and conductive carbon frameworks to mitigate severe volume fluctuations, facilitate rapid charge transfer, and efficiently capture K–pTe_n (K_5Te_3 and K_2Te) species through chemisorption. Despite encouraging results, the utilization of polar materials with distinct catalytic sites is still in its early stages, necessitating further scientific exploration. An unexplored avenue involves identifying swift and sustained chemical anchoring strategies to address the diverse K–pTe_n species. Moreover, constructing a suitable porous structure capable of accommodating volumetric stresses during the conversion reaction remains a crucial aspect for investigation. These research directions hold significant potential for advancing the performance and comprehension of electrocatalytic materials tailored for advanced PIBs. Specifically, metal catalysts, notably single-atom catalysts (SACs), have garnered considerable attention in Li–S or Se batteries, showcasing substantial improvements in the reaction kinetics of sulfur cathodes [32–35]. However, introducing an additional metal center to establish double active sites emerges as a promising strategy to further enhance the electrocatalytic conversion process. It is noteworthy that double active sites do not merely duplicate single atoms; they exhibit different catalytic characteristics, potentially unleashing a synergistic effect capable of surpassing the theoretical limit of SACs.

Based on the above discussion, we synthesize hollow porous carbon nanospheres (HPCNSs) through a straightforward wet–chemical process involving polymerization, carbonization, and subsequent removal of a silica (SiO_2) template. Consequently, we impregnated a homogeneous solution containing nickel (Ni) and cobalt (Co) as double atom catalysts (Ni/Co–DACs) within the HPCNSs through a drop–and–dry technique coupled with ultrasonication followed by carbonization, resulting in Ni/Co–N–HPCNS. Notably, nitrogen-doping (*N*-doping) into the nanostructure was introduced by adding a predetermined amount of urea during drop–and–dry process. It is noteworthy to mention that compared with other transition metal DACs, such as coupled Fe–Co and Fe–Fe, the synergistic effect of Ni and Co DACs revealed a dual-atom coupling effect causing charge redistribution and optimized coordination configuration, desired for high activity of Te [36]. Finally, the Ni/Co–N–HPCNS underwent treatment with Te powder in an inert atmosphere (N_2), ultimately producing Te–Ni/Co–N–HPCNS powder for use in K-ion storage. The inclusion of Ni/Co–DAC promotes the adsorption and electrocatalytic conversion of K–pTe_n species through efficient guiding and evolution of Te, enhancing the utilization of active material toward durable and safe K–Te batteries. Besides, the removal of SiO_2 accounts for the hollow cavity within the HPCNSs, which mitigates volume fluctuations and facilitates efficient electrolyte penetration, ensuring effective wetting of the electrode. Moreover, the presence of *N*-doping improves the conductivity of the synthesized nanostructure due to its more electronegative nature compared with the carbon [37–39]. Furthermore, DFT results highlight that the presence of Ni/Co–DAC results in stable

interactions with polytellurides, effectively eclipsing the shuttling of polytellurides between the positive and negative electrodes. Notably, the Ni/Co–N–HPCNS surface acts as an electron reservoir due to its excellent electrical conductivity and a much narrower band gap, enhancing the conductivity of the architecture and potentially catalyzing the redox reaction. Correspondingly, the cell employing Te–Ni/Co–N–HPCNS electrode demonstrates superior rate capability (up to 2.0 C) and ultra-high cycling performance at different C-rates of 0.5 C (600 cycles), 1.0 C (1800 cycles), and 2.0 C (3000 cycles). When employed as an anode material within a full-cell, the material demonstrates highly reversible K-ion electrochemistry. We believe that this work highlights a rational strategy of utilizing the Ni–Co DACs activity at the atomic level for the evolution of more resilient and innocuous K–Te batteries.

2 | Experimental

Tellurium-infiltrated hollow porous carbon nanospheres embedded with double-atom catalysts were prepared using a multistep process including polymerization, carbonization, template removal, Ni/Co infiltration, and Te impregnation. Initially, the hollow porous carbon nanospheres (HPCNSs) were prepared using an identical technique outlined in our previous work [29]. Thereafter, HPCNS powder was treated with a homogeneous solution containing 0.01 M Ni–salt ($Ni(CH_3COO)_2{\cdot}4H_2O$; $M_w = 248.86\%$, 97.0%, Daejung Chemicals & Metals Co. Ltd.) and Co–salt ($Co(CH_3COO){\cdot}4H_2O$; M_w = 249.08, > 98.0%, Daejung Chemicals & Metals Co. Ltd.) in ethanol using a drop-and-dry technique. Additionally, 0.5 M urea (NH_2CONH_2; M_w = 60.06, 99.0%, SAMCHUN) was used as a nitrogen source in the solution. The resulting black powder was then carbonized at 800°C for 3 h under N_2. The heating rate was fixed at 5°C min^{-1}. This crucial step ensures the reduction of metal acetates to respective metals distributed homogeneously at an atomic level. Thereafter, the obtained powder was gently mixed with tellurium (Te; M_w = 127.60, 99.8%, Aldrich) powder in a 1:1 mass ratio. The heating temperature was maintained at 350°C for 12 h under N_2. The obtained powder was designated as Te–Ni/Co–N–HPCNS. A control sample was also produced using the same process but without the double-atom catalyst, and named Te–HPCNS.

The detailed characterization techniques, along with the coin cell fabrication process and DFT calculations, are included in the supporting information.

3 | Results and Discussion

3.1 | Physical Characterization of the Prepared Powders

The detailed schematic illustration of the formation mechanism for Te–Ni/Co–N–HPCNS is presented in Scheme 1. Initially, a colloidal suspension comprising TEOS (Si–salt), resorcinol (R), and formaldehyde (F) was obtained by homogenously mixing these components in a blend of DI water, ethanol, and ammonia solution as a solvent. The resorcinol and formaldehyde form RF resin, whereas TEOS served as the source for the SiO_2 core. The RF resin underwent polymerization and condensed over the SiO_2 core (Scheme 1A). After 24 h of continuous stirring, the precipitates were collected through centrifugation and washed multiple times with DI water and ethanol. These precipitates were then subjected to a carbonization process at 700°C, resulting in the formation of a SiO_2 core surrounded by an RF-induced amorphous carbon nanosphere shell (SiO_2@CNS). The HPCNS were obtained from the SiO_2@CNS using an etching process using a 4.0 M NaOH solution. The etching removed the SiO_2 core, thereby forming micro- and mesopores along with a central hollow space. A standardized solution comprising Ni/Co–salts and urea in ethyl alcohol was entirely infused into the HPCNSs (Scheme 1B). Subsequently, the impregnated HPCNSs were heat-treated at 800°C for 3 h in a N_2 gas atmosphere. During this process, the Ni/Co–salts were converted into their respective metals, which were distributed homogeneously at the atomic level. Meanwhile, urea served as a source for forming *N*-doped carbonaceous species. This resulted in the formation of HPCNS impregnated with abundant Ni/Co heteronuclear double atom catalysts (Ni/Co–N–HPCNS). Finally, Te was infiltrated using a single-step heat-treatment performed at 350°C for 12 h in the presence of N_2 gas. The mass ratio of Te to Ni/Co–N–HPCNS was maintained at 1:1, culminating in the synthesis of Te–Ni/Co–N–HPCNS. A comparison sample, devoid of the abundant Ni/Co heteronuclear double atom catalysts, was also prepared using HPCNS as the host for Te impregnation using an identical procedure and abbreviated as Te–HPCNS (Scheme 1C).

The physical characterizations of the composite nanospheres, designated as SiO_2@RF and obtained immediately following the polymerization process, are illustrated in Supporting Information S1: Figure S1A–C. The FE–SEM image in Supporting Information S1: Figure S1A displays a uniformly spherical and nonaggregated morphology with a diameter of about 750 nm. The high magnification FE–SEM (Supporting Information S1: Figure S1B) shows a smooth surface of the nanosphere without deposits or accumulations. The XRD pattern in Supporting Information S1: Figure S1C displays only a broad peak at $2\theta = 22°$, highlighting the amorphous nature of the species formed during polymerization. The SiO_2@RF nanospheres underwent a carbonization step at 700°C for 5 h in an N_2 atmosphere, resulting in SiO_2@CNS, as shown in Supporting Information S1: Figure S1D–F. The morphological characteristics remain similar to those of the noncarbonized ones, with no significant differences. However, the average size (Supporting Information S1: Figure S1D,E) decreases to about 700 nm due to thermal contraction during the heat treatment. The XRD pattern (Supporting Information S1: Figure S1F) confirms the amorphous phase of the carbonized sample without impurity peaks. The carbonized SiO_2@CNS sample then underwent an etching process using a 4.0 M NaOH solution, followed by repeated washing with deionized water and ethanol, removing the SiO_2 core and resulting in hollow porous carbon nanospheres (HPCNSs), as depicted in Figure 1A–E. FE–SEM micrograph in Supporting Information S1: Figure S2A shows that the spherical morphology remains intact even after the etching process. Moreover, the TEM images (Supporting Information S1: Figure S2B and Figure 1A) firmly indicate the removal of the SiO_2 core, leading to a hollow core with a shell thickness of about 18 nm (Figure 1B). Notably, the shell primarily consists of carbonaceous species derived from the

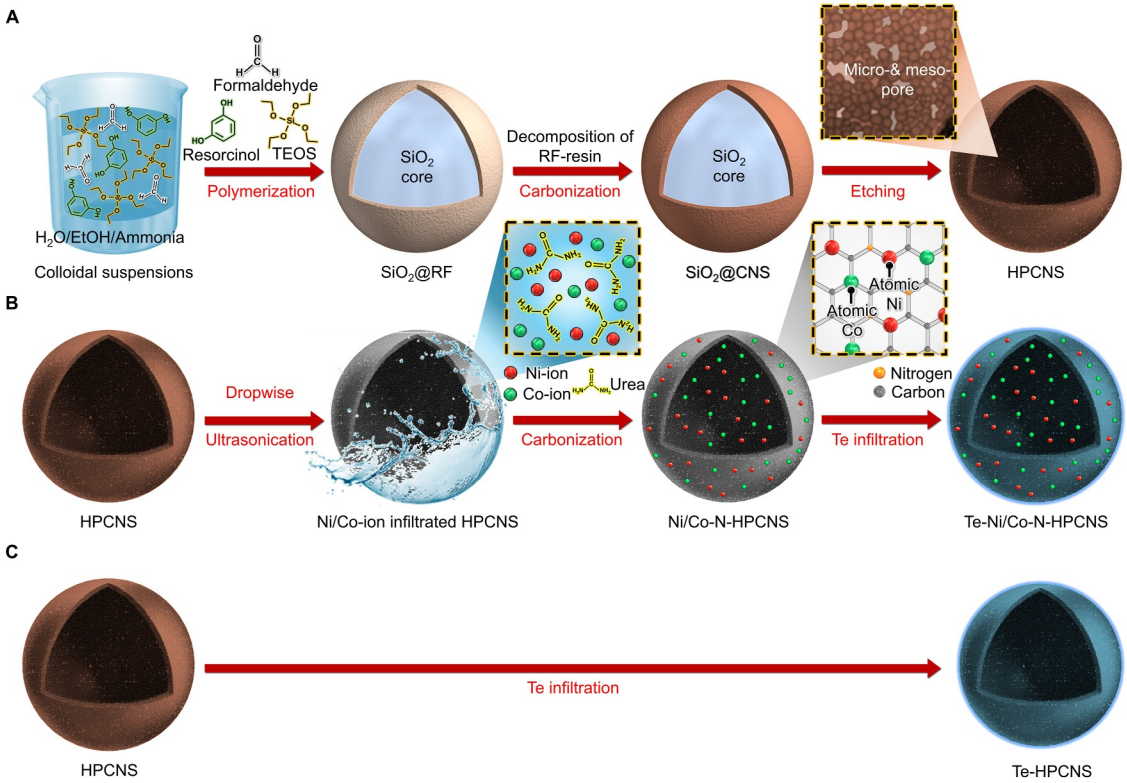

SCHEME 1 | Detailed formation mechanism of HPCNS as a host material. (A) Multi-step process, including polymerization, carbonization, and etching; (B) synthesis of Te–Ni/Co–N–HPCNS from HPCNS through impregnation, carbonization, and Te infiltration; (C) synthesis of Te–HPCNS for comparison.

carbonization of the RF resin. The selected area electron diffraction (SAED) and XRD pattern in Figure 1C,D, respectively, confirm the exclusive presence of an amorphous carbonaceous framework. Elemental mapping images (Figure 1E) also validate the presence of carbon, with a trivial amount of nitrogen, mainly introduced from the $-NH_3-$ molecules used as a solvent during synthesis. No other elemental impurities were detected. The HPCNS powder was then treated with a homogeneous solution of Ni/Co–salts in ethanol and a predetermined amount of urea as a nitrogen source. The solvent was finally evaporated, and the resulting powder was carbonized at 800°C for 3 h in an N_2 atmosphere. This high-temperature carbonization ensures the reduction of metal acetates to their respective metals, uniformly distributed within the carbon shell of the HPCNSs at an atomic level. The physical results of the obtained powder are shown in Figure 1F–J. FE–SEM (Supporting Information S1: Figure S2C) and TEM images (Supporting Information S1: Figure S2D and Figure 1F) reveal no substantial alterations in the morphology of the nanospheres. The high-angle annular dark-field scanning transmission electron microscopy (HAADF-STEM) image in Figure 1G shows a uniform distribution of Ni and Co within the nanostructure. Inductively coupled plasma atomic emissions spectroscopy (ICP-AES) quantifies the Ni and Co content at nearly equal proportions (approximately 0.24 wt%). SAED pattern shown in Figure 1H reveals diffraction patterns analogous to the amorphous carbonaceous species. XRD pattern (Figure 1I) also reveals broad peaks corresponding to carbonaceous species only with no traces of Ni and Co owing to their low proportions. However, during the synthesis, a high concentration of Ni and Co salt (0.05 M) resulted in the formation of a Ni and Co metallic phase, as evidenced by XRD (Supporting Information S1: Figure S3). Furthermore, the elemental dot mapping images in Figure 1J firmly indicate the homogeneous distribution of abundant Ni/Co double atom catalysts (DACs) within the carbon shell. Besides, the consistent elemental dot density indicates identical proportions at an atomic scale within the prepared nanostructure. Consequently, the synthesized powder was abbreviated as Ni/Co–N–HPCNS.

The synthesized Ni/Co–N–HPCNS powder served as a host for tellurium (Te) loading using a single-step heat-treatment at 350°C for 12 h in an N_2 atmosphere. Subsequently, the resulting material, designated as Te–Ni/Co–N–HPCNS, underwent comprehensive characterization, as depicted in Figure 2. FE–SEM micrographs in Figure 2A,B demonstrated that the spherical morphology was preserved following Te infiltration. Besides, no bulky Te deposits (Figure 2B) were observed on the HPCNS surface, suggesting an efficient impregnation process. XRD pattern in Figure 2C correlates well with the FE–SEM observations, displaying a broad peak at approximately $2\theta = 22°$ associated with carbonaceous material, whereas a few low-intensity peaks signal the presence of surface Te. Notably, increasing the mass ratio of Te to the host powder to 2:1 produced more distinct XRD peaks indicative of Te phases, signifying a greater quantity of bulk Te deposits on the HPCNS surface (Supporting Information S1: Figure S4). Additionally, the impregnation achieved maximum efficiency at 350°C, outperforming other temperatures, as shown in Supporting Information S1: Figure S5. Notably, temperatures above 350°C

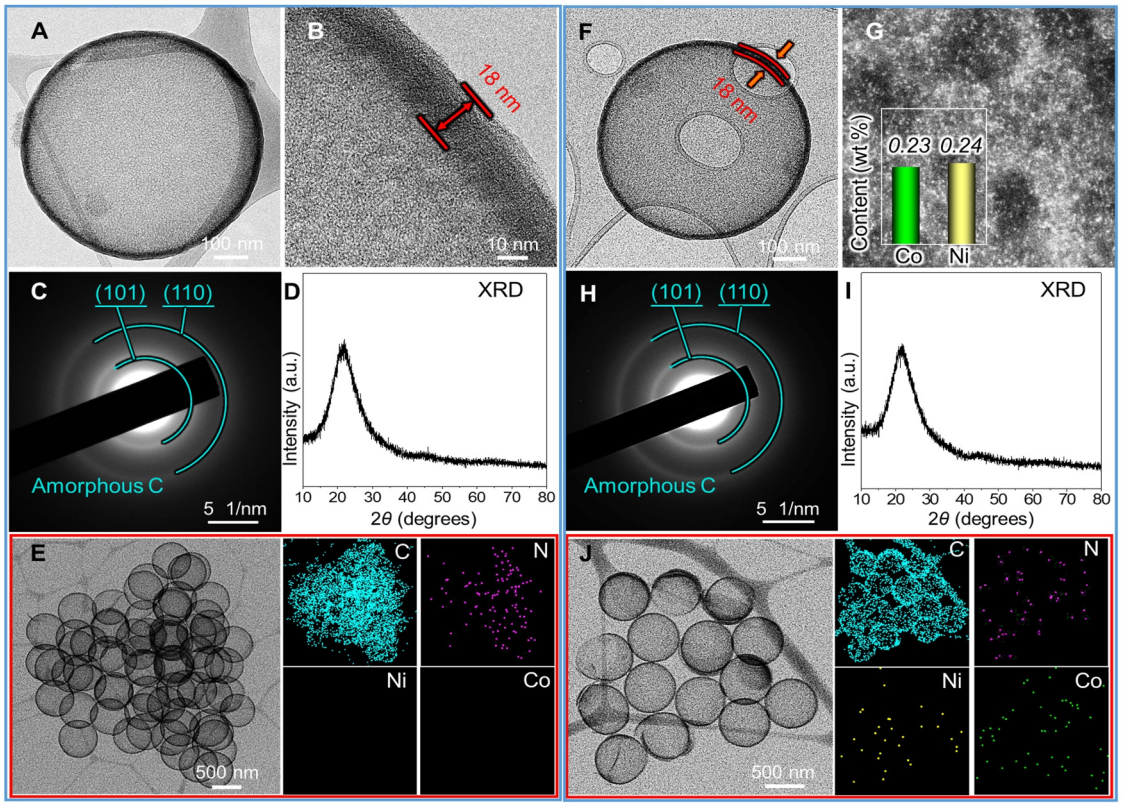

FIGURE 1 | Physical characterization of the HPCNS post-etching of carbonized SiO_2@CNS powder and Ni/Co–N–HPCNS achieved through a drop–and–dry technique combined with ultrasonication, followed by carbonization at 800°C in an N_2 atmosphere includes: (A,F) TEM images, (B) HR–TEM image, (G) HAADF–STEM image with an inset showing the ICP content for Co and Ni, (C,H) SAED pattern, (D,I) XRD patterns, and (E,J) elemental dot mapping images.

resulted in minimal Te infiltration, whereas lower heating temperatures caused a high percentage of surface Te. The low- and high-magnification TEM images in Figure 2D,E, respectively, also revealed no bulky Te deposits on the surface. The HR–TEM image (Figure 2F) and SAED pattern (Figure 2G) indicate no clear lattice fringes or diffraction rings associated with the infiltrated Te, confirming its amorphous nature. To further endorse this, Raman spectra of Te–Ni/Co–N–HPCNS and elemental Te were compared and are presented in Figure 2H. No Raman peaks corresponding to Te were observed for Te–Ni/Co–N–HPCNS, whereas the elemental Te powder displayed Raman peaks at 113.8, 134.3, and 260.2 cm^{-1} associated with Te-Te bonds [40, 41]. Additionally, an I_D/I_G value of 1.02 indicates the amorphous characteristics of the carbonaceous species [42]. The amount of infiltrated Te within the prepared powder was quantified using a TG curve (Figure 2I) in an N_2 atmosphere and was found to be approximately 48.5 wt%. Elemental mapping images (Figure 2J) further disclose a homogenous distribution of C, N, and Te within the prepared nanostructure. Besides, the presence of abundant Ni/Co heteronuclear dual sites as catalysts is also evident. These results indicate the successful synthesis of Te–Ni/Co–N–HPCNS. To highlight the nanostructure advantages, a comparison sample utilizing Te-infiltrated HPCNS without abundant DAC heteronuclear dual sites was also prepared. The detailed characterizations followed by respective discussions are presented in Supporting Information S1: Figure S6.

The electronic state and bonding environment were characterized using the X-ray photoelectron spectroscopy (XPS) technique. XPS survey spectrum shown in Figure 3A identifies the electronic states of C 1s, N 1s, Te 3p, and Te 3d. Notably, the photoelectron peaks for Co 2p and Ni 2p were absent, confirming their low concentrations. The high magnification spectrum in Figure 3B displays pronounced peaks at 821.9 and 873.2 eV, attributed to the Te $3p_{3/2}$ and Te $3p_{1/2}$ orbital states, respectively, which suggests Te infiltration within the nanostructure [1]. The C 1s XPS spectra in Figure 3C reveal three distinct profiles associated with different bonding orbitals: –C=C– (283.9 eV), –C–C–/C–N– (284.9 eV), and –C–O– (287.2 eV) [43, 44]. The dominant –C=C– peak strongly supports the presence of a carbonaceous framework [45, 46]. This is consistent with the deconvoluted N 1s XPS spectrum in Figure 3D, which features four fitted photoelectron peaks associated with different nitrogen environments: pyridinic N (397.8 eV), pyrrolic N (400.1 eV), graphitic N (401.9 eV), and oxidized N (404.6 eV) [47, 48]. The high-resolution C 1s and N 1s spectra firmly validate the formation of an *N*-doped carbonaceous framework, marked by numerous surface defects primarily induced by high levels of *N*-doping. These findings are reinforced by EA results (Supporting Information S1: Table S1), showing carbon and nitrogen contents of approximately 43.9 wt% and 1.9 wt%, respectively, within the nanostructure. Furthermore, the Te–Ni/Co–N–HPCNS exhibits a BET surface area of 145 $m^2\ g^{-1}$ (Figure 3E), which is lower than that of Ni/

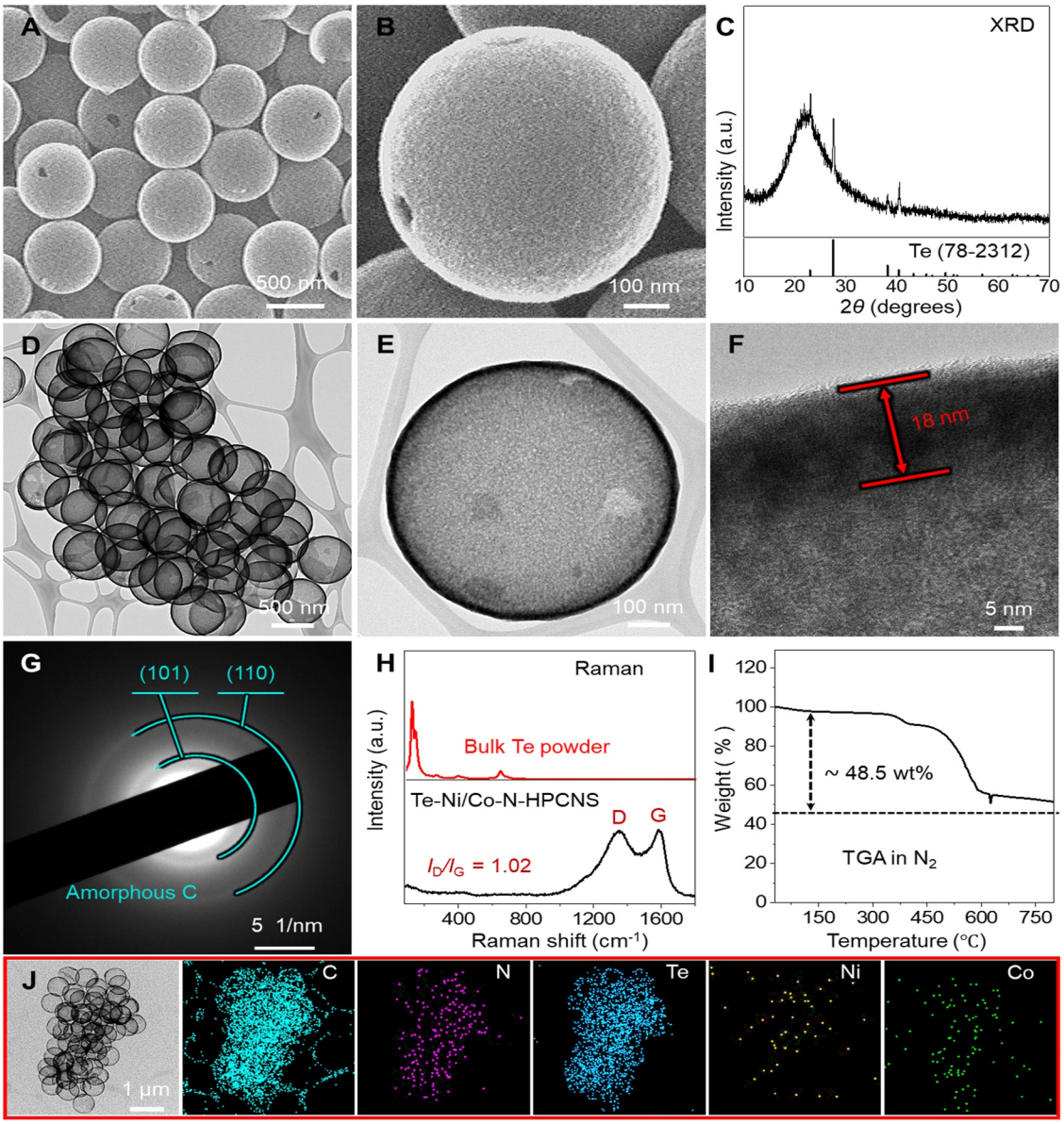

FIGURE 2 | Physical characterization of the Te–Ni/Co–N–HPCNS obtained at 350°C in an N_2 atmosphere includes: (A,B) FE–SEM micrographs, (C) XRD pattern, (D,E) TEM images, (F) HR–TEM image, (G) SAED pattern, (H) Raman spectra, (I) TG curve, and (J) elemental dot mapping images.

Co–N–HPCNS (502 $m^2\ g^{-1}$) and HPCNS (629 $m^2\ g^{-1}$; Supporting Information S1: Figure S7A), indicating the infiltration of Te into the porous structure. This observation is reinforced by pore size distribution (BJH curve; Figure 3F), showing a reduced volume density of micro- and mesopores compared to the nonfilled sample. Importantly, the porous structure facilitates diffusion of charged species by decreasing the diffusion stretch, while also harmonizing volume fluctuations, thereby enhancing overall electrochemical performance.

3.2 | Electrochemical Performance of the Prepared Nanostructure

Encouraged by captivating physical outcomes, we commenced a detailed electrochemical examination of the prepared nanostructure. Utilizing CR2032 coin cells containing Te–Ni/Co–N–HPCNS and Te–HPCNS electrodes paired with metallic-K, we conducted cyclic voltammetry (CV) tests initially at a scan rate of 0.1 mV s^{-1}, as depicted in Figure 4A–C. The first CV scan shown in Figure 4A featured broad and intense peaks at 0.87 and 0.91 V for Te–Ni/Co–N–HPCNS and Te–HPCNS, respectively, corresponding to the irreversible insertion of K-ions into the carbon matrix and the reduction of Te to form K_xTe species [28]. Subsequent cathodic scans (Figure 4B,C), however, displayed new peaks at 1.85 V, along with distinct peaks at 1.46 and 0.97 V, indicating the stepwise reduction of Te. Similarly, the anodic peaks observed during the first and successive scans at 1.68, 2.02, and 2.29 V for both samples illustrated reversible electrochemical processes involving the extraction of K-ions and the oxidation of Te [5]. Notably, high redox intensity values for the Te–Ni/Co–N–HPCNS electrode suggest better utilization of the active material. Furthermore, precisely overlapping CV profiles indicated highly reversible K–Te electrochemical processes within the assembled cells. Moreover, the cell utilizing the Te–Ni/Co–N–HPCNS electrode demonstrated superior rate

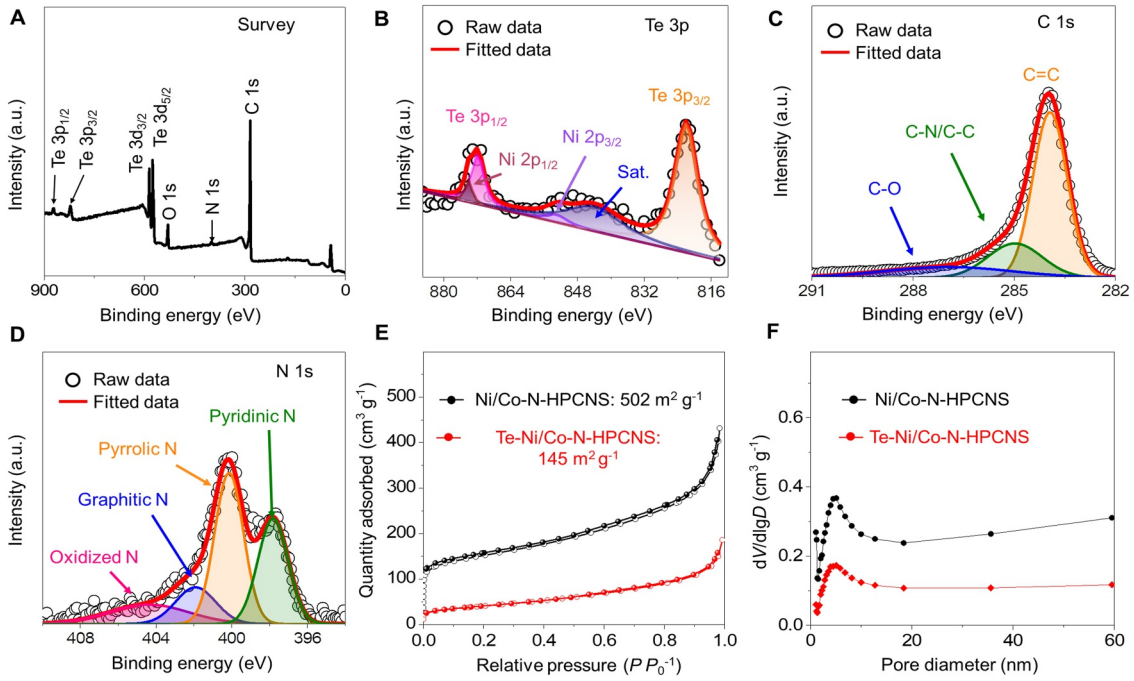

FIGURE 3 | XPS analysis of the Te–Ni/Co–N–HPCNS along with the BET comparison. (A) Survey spectrum, (B) Te 3p XPS spectrum, (C) C 1s XPS spectrum, (D) N 1s XPS spectrum, (E) N_2 adsorption-desorption isotherms, and (F) BJH desorption pore-size distribution.

performance at various current rates (1C = 420 mAh g^{-1}) from 0.05–2.0 C, as illustrated in Figure 4D. The cell delivered initial discharge capacities of 566 (second cycle), 493, 438, 403, 349, 305, 297, and 238 mAh g^{-1} at 0.05C, 0.1C, 0.2C, 0.3C, 0.5C, 0.7C, 1.0C, and 2.0C, respectively. Despite a high C-rate of 2.0 C, the cell maintained 56.6% of the theoretical value. Moreover, the capacity value recovered when the current returned to 0.1 C, affirming the reversibility of the electrochemical processes within the cell. In contrast, the cell using the Te–HPCNS electrode exhibited lower discharge capacities of 406 (second cycle), 333, 295, 279, 260, 236, 217, and 181 mAh g^{-1} at 0.05C, 0.1C, 0.2C, 0.3C, 0.5C, 0.7C, 1.0C, and 2.0C, respectively. Notably, the cell featuring the two electrodes exhibited an extraordinary initial discharge capacity for the initial cycle at 0.05C, as shown in Supporting Information S1: Figure S8. This primarily resulted from irreversible capacity contributions from the DAC@HPCNS or HPCNS framework during the initial cycle, in addition to the formation of a solid electrolyte interphase, consistent with previous reports [28]. To quantify the capacity contribution from the Ni/Co–N–HPCNS or HPCNS framework, cells were assembled utilizing Ni/Co–N–HPCNS or HPCNS versus K configuration and cycled at a current density of 20 mA g^{-1}, as presented in Supporting Information S1: Figure S9. The cell featuring Ni/Co–N–HPCNS (Supporting Information S1: Figure S9A,B) or HPCNS (Supporting Information S1: Figure S9C,D) initially delivered discharge capacities of 874/807 mAh g^{-1}, respectively. After 100 cycles, the capacity stabilized at 120/132 mAh g^{-1}, highlighting minimal degradation during long-term cycling. The galvanostatic charge–discharge voltage profiles at different C-rates, presented in Figure 4E,F is consistent with CV outcomes. The notable discharge capacities at high C-rates for the Te–Ni/Co–N–HPCNS electrode reflect improved reaction kinetics within the cell. This improvement is mainly attributed to the presence of abundant Ni/Co heteronuclear dual sites acting as catalysts, which promote the efficient electrocatalytic conversion of intermediate K–pTe_n species, resulting in an enhanced utilization of the active material. Additionally, the hollow porous carbon scaffold offers short diffusion pathways for charged species, resulting in fast charge transfer kinetics.

The cycling performance of a material is a crucial factor in determining its viability for wide-scale applications. Therefore, the electrochemical performance was further supplemented using long-term cycling tests at different C-rates, as depicted in Figure 4G. Notably, cells featuring Te–Ni/Co–N–HPCNS and Te–HPCNS electrodes were initially cycled for a few cycles at low C-rates. As observed, the cell paired with the Te–Ni/Co–N–HPCNS electrode exhibited a discharge capacity of 319 mAh g^{-1} (fifth cycle) at 0.5C and retained nearly 69% (221 mAh g^{-1}) of the capacity at the 600^{th} cycle. This resulted in an average capacity attenuation of just 0.05% per cycle, revealing high active material utilization. Similar performance was depicted even at higher C-rates of 1.0C (Supporting Information S1: Figure S10) and 2.0C during ultra-long cycling tests. As shown, the cell exhibits a discharge capacity of 217 mAh g^{-1} (sixth cycle) at 1.0C and retains almost 68% (148 mAh g^{-1}) of the capacity at the 1800^{th} cycle with an average capacity attenuation of 0.01% per cycle. Likewise, when cycled at a C-rate of 2.0C, the Te–Ni/Co–N–HPCNS electrode retained almost 60% (144 mAh g^{-1} considered after the 10th cycle) of the capacity at the end of the 3000th cycle, resulting in a capacity decay rate of only 0.01% per cycle. Notably, the discharge capacity patterns at 0.5C, 1.0C, and 2.0C reveal an increase in capacity values during the first few tens of cycles, primarily due to an activation process. Furthermore, high Coulombic efficiency (CE) values of 100.4% and 100.0% at 0.5 and 2.0C, respectively, demonstrate highly reversible K–Te electrochemical reactions. It is also noteworthy

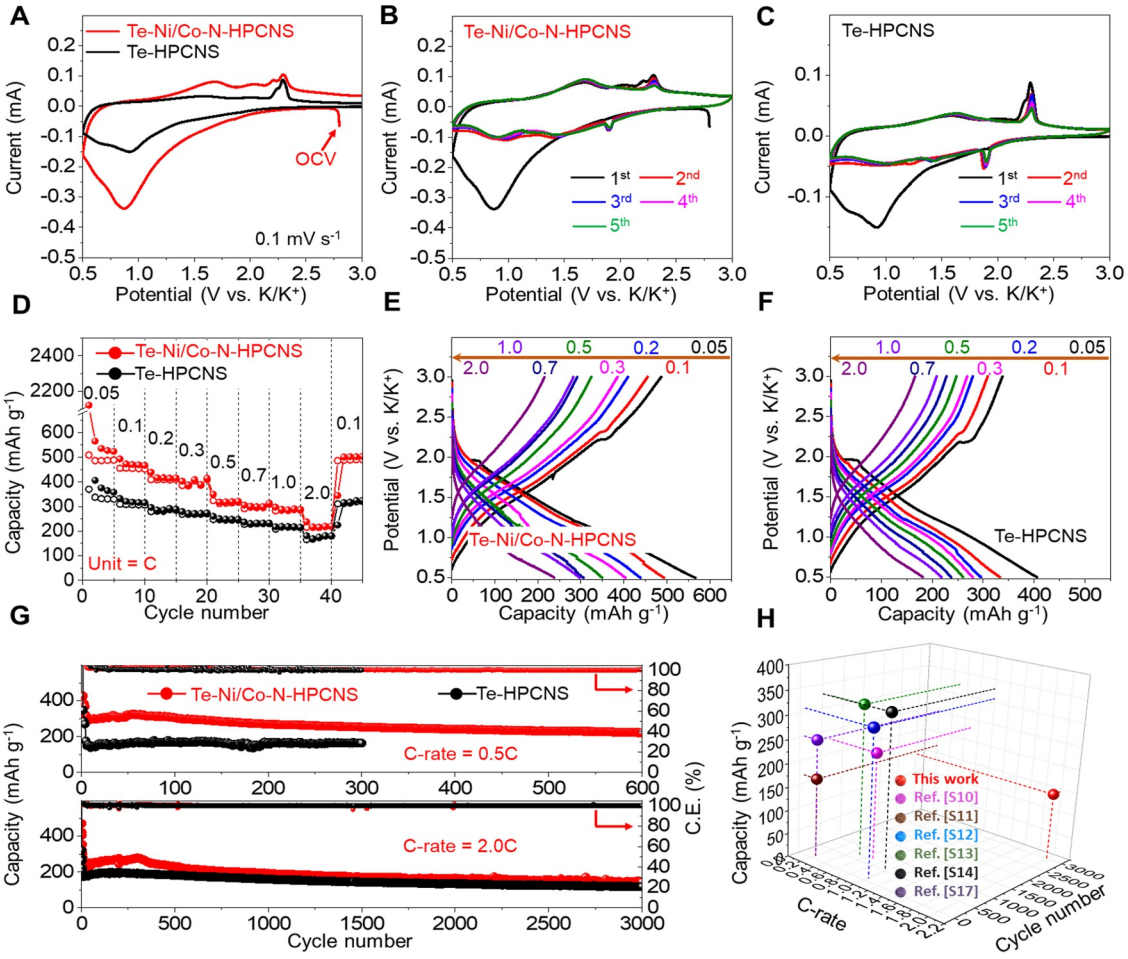

FIGURE 4 | Electrochemical performance of Te–Ni/Co–N–HPCNS and Te–HPCNS for K-ion storage includes. (A) Comparison of the first CV scan at 0.1 mV s^{-1}, (B) first five CV scans for Te–Ni/Co–N–HPCNS at 0.1 mV s^{-1}, (C) first five CV scans for Te–HPCNS at 0.1 mV s^{-1}, (D) rate capability tests at different C-rates ranging from 0.05C to 2.0C, (E) galvanostatic voltage profiles for Te–Ni/Co–N–HPCNS at different C-rates, (F) galvanostatic voltage profiles for Te–HPCNS at different C-rates, (G) cycling performance at a 0.5C and 2.0C, and (H) a comparative analysis of electrochemical performance with previous studies.

that the cell featuring the Te–Ni/Co–N–HPCNS electrode exhibited an average discharge voltage of ~1.2 V (Supporting Information S1: Figure S11) during cycling at 0.5C, which is comparable to other metal–sulfur (K–S; ~1.2 V) and metal–selenium (K–Se; ~1.4 V) battery systems [49, 50]. To the best of our knowledge, the remarkable cyclability of the Te–Ni/Co–N–HPCNS electrode is superior or comparable with previously reported Te–based materials in the K-ion battery system, as shown in Figure 4H and Supporting Information S1: Table S2. The astonishing cycling performance of the Te–Ni/Co–N–HPCNS electrode confirms that its structural advantages not only improve the utilization of the active material through efficient catalytic conversion of pTe_n species but also promote enhanced redox kinetics within the electrode. In contrast, the cell utilizing the Te–HPCNS electrode delivered low discharge capacity values at both 0.5C (163 mAh g^{-1} after 300 cycles) and 2.0C (118 mAh g^{-1} after 3000 cycles), indicative of minimal active material involvement in the redox processes. This is primarily due to the relatively poor conversion of pTe_n, resulting in material loss and, hence, comparatively sluggish electrochemical performance.

To gain deeper insights into the exceptional K-ion storage performance of the Te–Ni/Co–N–HPCNS electrode, CV curves at different scan rates, EIS curves during cycling, and GITT were performed. As evident from Figure 5A,C, CV curves at all voltage scan rates (i.e., 0.2, 0.3, 0.4, and 0.5 mV s^{-1}) exhibit similar redox peaks as discussed under Figure 4A–C. Additionally, the intensity of redox peaks for the Te–Ni/Co–N–HPCNS electrode increases monotonically with an increase in scan rates, indicating more active material utilization compared to the Te–HPCNS electrode, in which redox intensity also increases but to a lesser extent. It is worth noting that the potential differences between the cathodic (marked as *R*) and anodic peaks (marked as *O*) at scan rates of 0.2, 0.3, 0.4, and 0.5 mV s^{-1} were 0.71/0.74, 0.98/0.86, 1.09/1.15, and 1.21/1.24 V for the Te–Ni/Co–N–HPCNS and Te–HPCNS electrodes, respectively. This suggests that the presence of Ni/Co heteronuclear dual sites as catalysts significantly mitigates electrochemical polarization, possibly catalyzing redox reactions, and thereby rendering the electrode reactions much more reversible. Furthermore, the diffusion kinetics involving the Te–Ni/Co–N–HPCNS electrode was evaluated using the Randles–Sevcik equation:

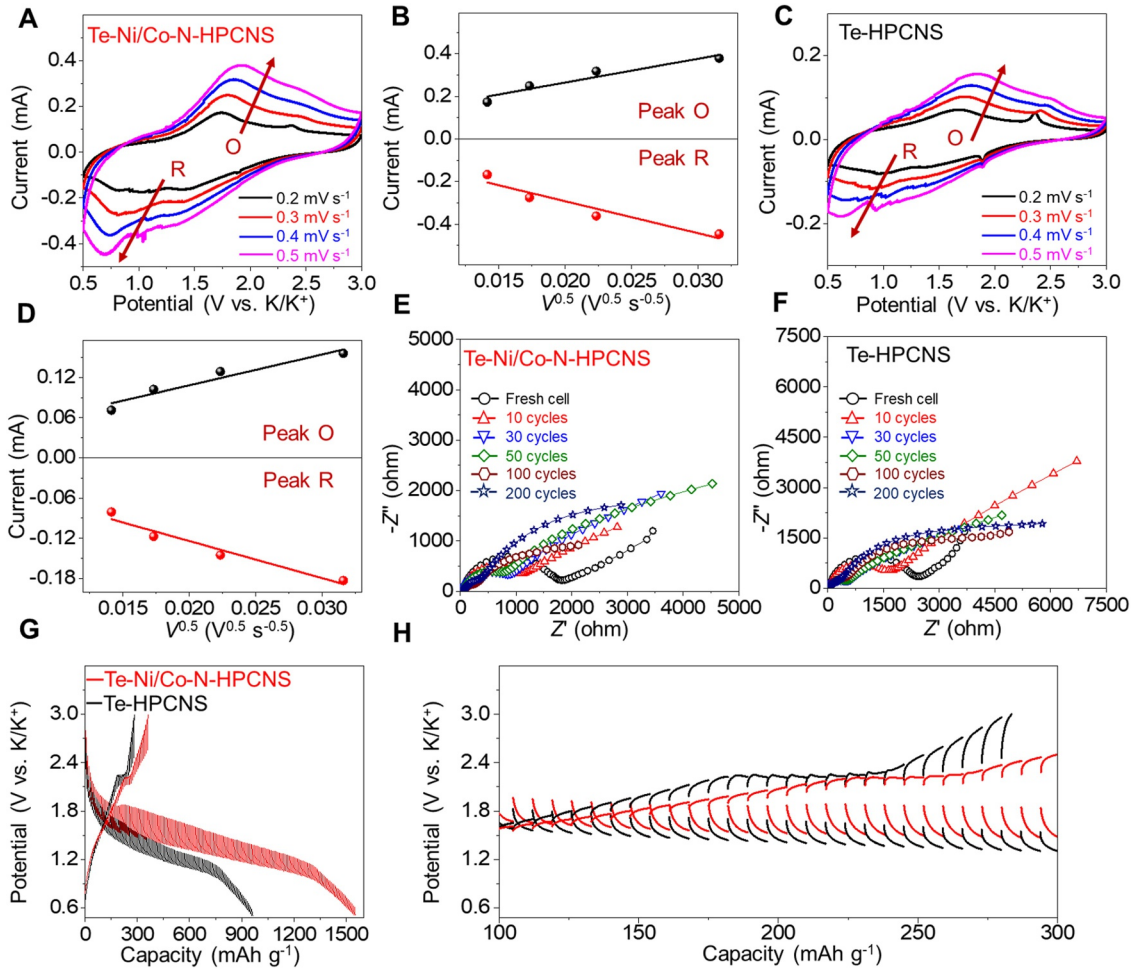

FIGURE 5 | K-ion redox kinetics analysis for cells utilizing Te–Ni/Co–N–HPCNS and Te–HPCNS. (A,C) CV curves at different scan rates ranging from 0.2 to 0.5 mV s^{-1}, (B,D) peak current versus square root of the voltage scan rate plots for reduction and oxidation peaks, (E,F) Nyquist plots at different cycle numbers at 2.0C-rate, and (G,H) GITT tests for the initial cycle at 0.05C.

$$I_p = 2.69 \times 10^5 n^{1.5} A D_{K^+}^{0.5} C \nu^{0.5}, \quad (1)$$

where all the parameters have typical meanings. $D_K{}^{+0.5}$ was obtained from I_p versus $\nu^{0.5}$ slope for the two redox peaks, as shown in Figure 5B,D. The Te–Ni/Co–N–HPCNS electrode exhibits an order of magnitude higher $D_K{}^+$ value for peak *R* (4.9×10^{-10} cm^2 s^{-1}) and peak O (2.7×10^{-10} cm^2 s^{-1}) compared with the Te–HPCNS electrode (peak R: 6.7×10^{-11} cm^2 s^{-1}; and peak O: 4.6×10^{-11} cm^2 s^{-1}), suggesting faster K-ion diffusion characteristics within the electrode. Notably, these diffusion values surpass those reported in previous studies on K–Te battery systems, affirming a robust structural design strategy [51]. These results align well with the EIS data obtained during cycling at 2.0 C (Figure 5E,F). In addition, a lower R_e and R_{ct} values for the Te–Ni/Co–N–HPCNS electrode were obtained compared to the Te–HPCNS electrode. For instance, the R_{ct} values at the end of the 200th cycle were 489 versus 626 Ω for the Te–HPCNS electrode, specifying lethargic electrochemical reactions. In addition, the GITT (Figure 5G,H) shows that the voltage variations during K-ion insertion/de-insertion processes in Te–Ni/Co–N–HPCNS electrode are noticeably smaller than those in Te–HPCNS electrode, validating amended K-ion redox chemistry and superior charge-transfer features.

3.3 | Redox Reaction Mechanism for K-Ion Storage

To elucidate the superior redox mechanism responsible for the exceptional K-ion storage performance of the Te–Ni/Co–N–HPCNS electrode, we conducted in situ and ex-situ XRD and TEM analyses of the cycled electrodes, followed by XPS at different charge–discharge voltages (Figure 6). The in situ XRD results presented in Figure 6A reveal no significant differences. However, noticeable peaks corresponding to BeO (38.6°), pure Be (45.9°, 51.0°, and 52.8°), and Al (44.4° and 65.2°) were observed. The corresponding magnified contour plot in Figure 6B demonstrates considerable changes. For instance, at the initial stage of the discharge process, intense characteristic peaks appeared at 17.2°, 24.1°, 25.7°, and 28.6°, corresponding to the formation of the K_2Te_3 phase (JCPDS No. 71-0490; Orthorhombic; *Pnma*). However, the continuous fading of peak intensity during further discharge indicates a gradual transformation into other polytelluride species, more preferably to K_5Te_3. This perception aligns with the ex-situ XRD pattern shown in Figure 6C. As is evident, the XRD revealed peaks associated with impregnated amorphous Te only at the open-circuit voltage (OCV). As potassiation progresses (OCV to

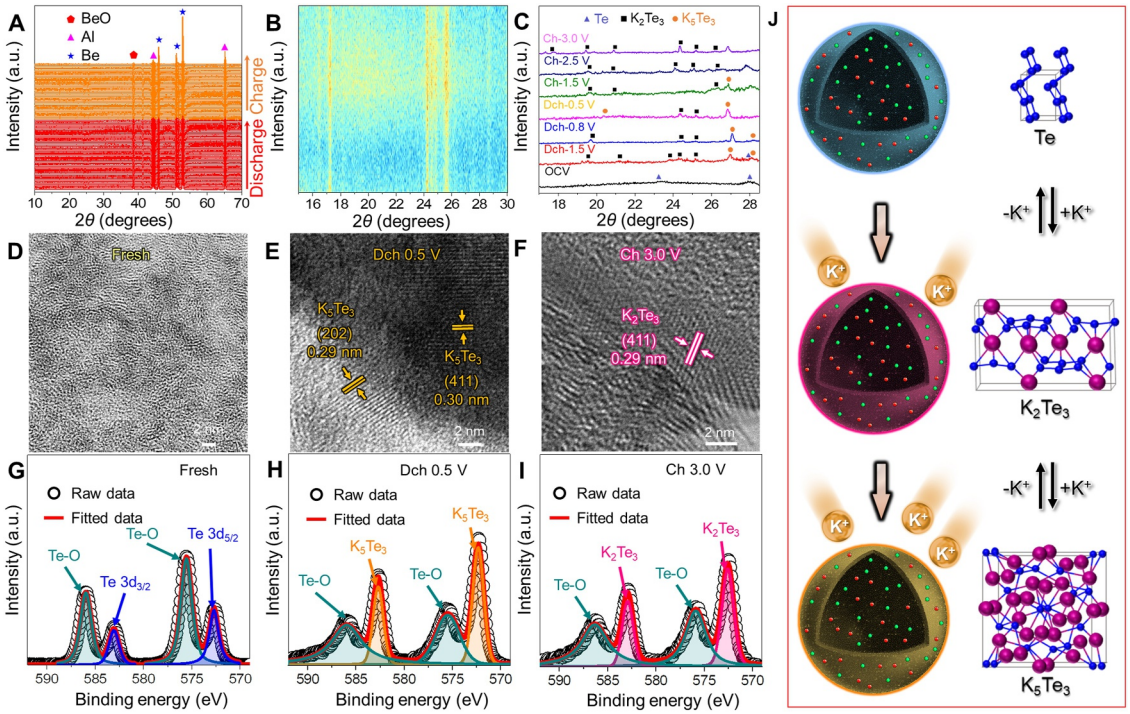

FIGURE 6 | In situ/ex-situ XRD, HR-TEM, and XPS analysis of the Te–Ni/Co–N–HPCNS electrode during first cycle. (A) In situ XRD of the Te–Ni/Co–N–HPCNS electrode during the first cycle at 0.2C; (B) corresponding 2D contour plot; (C) ex-situ XRD patterns at different discharge and charge stages; HR–TEM images of (D) fresh electrode, (E) electrode discharged to 0.5 V, and (F) electrode charged to 3.0 V; de-convoluted Te 3d XPS spectra at different state of discharge and charge: (G) fresh electrode, (H) discharged to 0.5 V, and (I) charged to 3.0 V; and (J) schematic illustration of the K-ion storage mechanism in the Te–Ni/Co–N–HPCNS electrode.

1.5 V), peaks corresponding to the K_2Te_3 phase appear alongside those of the K_5Te_3 phase (JCPDS No. 79-1056; Tetragonal; $I4/m$) and residual Te phase. Further potassiation (1.5–0.8 or 0.5 V) shows peaks corresponding to the K_5Te_3 phase growing at the expense of the K_2Te_3 phase. During the reverse scan (de-potassiation), the results in Figure 6B,C are well synchronized. The peaks at 24.5° and 24.8° in Figure 6B are initially low during the discharge, increase monotonically, and reach a maximum at the end of discharge. As the polarity reverses, the signal strength continuously fades, reverting to the state observed at OCV. These peaks are attributed to the K_5Te_3 phase. Conversely, the peaks at 17.2° and 28.6° become more prominent during the initial charging process, indicating the formation of the K_2Te_3 phase. The ex-situ XRD in Figure 6C also shows the continuous weakening of peaks corresponding to the K_5Te_3 phase as the K_2Te_3 phase forms during charging. HR–TEM images were obtained for uncycled (fresh), fully discharged, and charged electrodes to authenticate the XRD results. The HR–TEM image of the uncycled electrode in Figure 6D reveals no distinct lattice fringes, confirming the amorphous nature of the impregnated Te within the carbonaceous framework. When fully discharged to 0.5 V (Figure 6E), diffraction lattice fringes corresponding to the (202) and (411) crystal planes were observed, indicating potassiation of Te to K_5Te_3. Likewise, the HR–TEM image for the fully charged electrode (3.0 V; Figure 6F) shows lattice fringes attributed to the (411) plane of the K_2Te_3 phase, confirming the transformation of K_5Te_3 during de-potassiation. Ex situ XPS spectra were also obtained to supplement the above results. The deconvoluted spectra for Te 3d in Figure 6G reveal well-fitted photoelectron signals centered at 572.7 and 583.1 eV, corresponding to the Te $3d_{5/2}$ and Te $3d_{3/2}$ electronic orbitals, respectively [52]. Additionally, the peaks at 575.5 and 585.9 eV could be assigned to Te–O species formed due to the surface oxidation of the specimen during measurement [53]. After being discharged to 0.5 V, peaks corresponding to the Te $3d_{5/2}$ and Te $3d_{3/2}$ electronic orbitals were observed at the slightly reduced binding energy values of 572.3 and 582.6 eV, respectively, indicating alterations in the Te environment owing to the chemical interactions between Te and K that form K_5Te_3 [28]. In contrast, upon recharging to 3.0 V, characteristic photoelectron signals for K_2Te_3 were detected at 572.5 eV (Te $3d_{5/2}$) and 582.8 eV (Te $3d_{3/2}$). Notably, the intensities of K–Te bonds (Figure 6H,I) were much higher than those of Te–O bonds, suggesting increased electrochemical activity. Based on the in situ and ex-situ XRD, along with HR–TEM and XPS results, a schematic illustration of the involved redox mechanism and phase transformation is presented in Figure 6J.

3.4 | Computational Insights for Polytelluride Dissolution

Density function calculations were further conducted to investigate the dissolution of K–pTe$_n$ species during K-ion storage using different optimized structures. These optimized structures primarily consist of *N*-doped graphitic carbon (N_3G) and M@N_3G (M = Ni/Co, Ni, and Co) surfaces. The (7 × 7) N_3G (001) surface, which comprises 94 C and 3 N atoms, was modeled from the bulk carbon structure that includes two C atoms with lattice parameters ($a = b = 2.45$ Å, $c = 8.39$ Å,

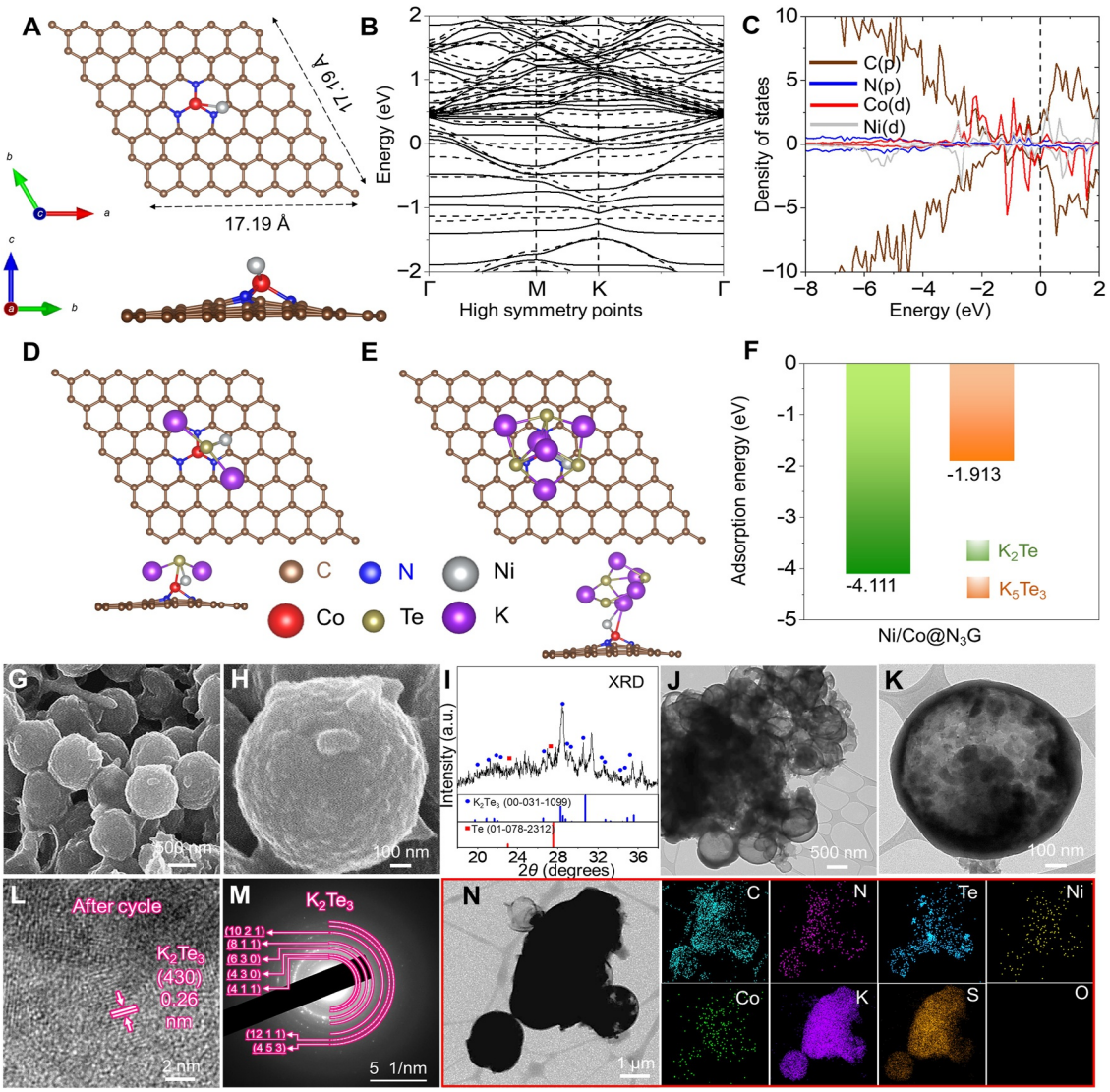

FIGURE 7 | Computational insights and after cyling analysis of the Te–Ni/Co–N–HPCNS. (A) Top and side views of the pristine optimized (7 × 7) Ni/Co@N_3G (001) surface; (B) band structures, (C) PDOS on the pristine (7 × 7) Ni/Co@N_3G (001) surface; (D,E) K_2Te and K_5Te_3 adsorbed on the (7 × 7) Ni/Co@N_3G (001) surface; (F) adsorption energies of K_2Te and K_5Te_3 on the pristine (7 × 7) Ni/Co@N_3G (001) surface; physical characterization of the cycled electrode: (G,H) FE–SEM images, (I) XRD pattern, (J,K) TEM images, (L) HR–TEM image, (M) SAED pattern, and (N) elemental dot mapping images.

$\alpha = \beta = 90°$, $\gamma = 120°$). This surface represents the most stable (001) crystallographic facet and features the highest intensity peak at $2\theta = 10.54°$ in the simulated XRD pattern, as depicted in Supporting Information S1: Figure S12. Considering the size of adsorbates such as K_2Te and K_5Te_3, the (7 × 7) N_3G (001) surface was modeled by extending the distance to 17.19 Å along both the *x*- and *y*-axis, with a vacuum space of 20 Å on the *z*-axis to minimize periodic image interactions in adjacent cells (Supporting Information S1: Figure S13A). Besides, the (7 × 7) M@N_3G (001) surfaces, where *M* represents Ni/Co, Ni, and Co, were also optimized to understand the adsorption energetics of K_2Te and K_5Te_3, as shown in Figure 7A, Supporting Information S1: Figures S14A, and S15A, respectively. Moreover, band structure calculations were performed for different optimized surfaces along high symmetry k-points (G-M-K-G). The (7 × 7) Ni@N_3G (001) surface exhibited a direct band gap of 0.017 eV (Supporting Information S1: Figure S14B), with the valence band maximum (VBM) at −0.009 eV and the conduction band minimum (CBM) at 0.008 eV, both located at the k-point (0.0, 0.0, 0.0). Similarly, the (7 × 7) Co@N_3G (001) surface exhibited a direct band gap of 0.012 eV (Supporting Information S1: Figure S15B), with the VBM at −0.003 eV and the CBM at 0.009 eV, both at the k-point (0.0, 0.0, 0.0). Interestingly, the (7 × 7) Ni/Co@N_3G (001) surface exhibited the narrowest direct band gap of 0.004 eV (Figure 7B), with both the VBM and CBM at 0.0 and 0.004 eV, respectively, located at the k-point (0.0, 0.0, 0.0). Consequently, the band structure analysis indicates that the (7 × 7) N_3G (001)-optimized surface grafted with Ni/Co–DAC exhibits enhanced electrical conductivity with a narrower band gap compared to the surfaces grafted solely with Ni or Co–SAC, thus bringing the valence and conduction bands closer to the Fermi level. Projected density of states (PDOS) calculations were also conducted for all optimized surfaces, as depicted in Figure 7C, Supporting Information S1:

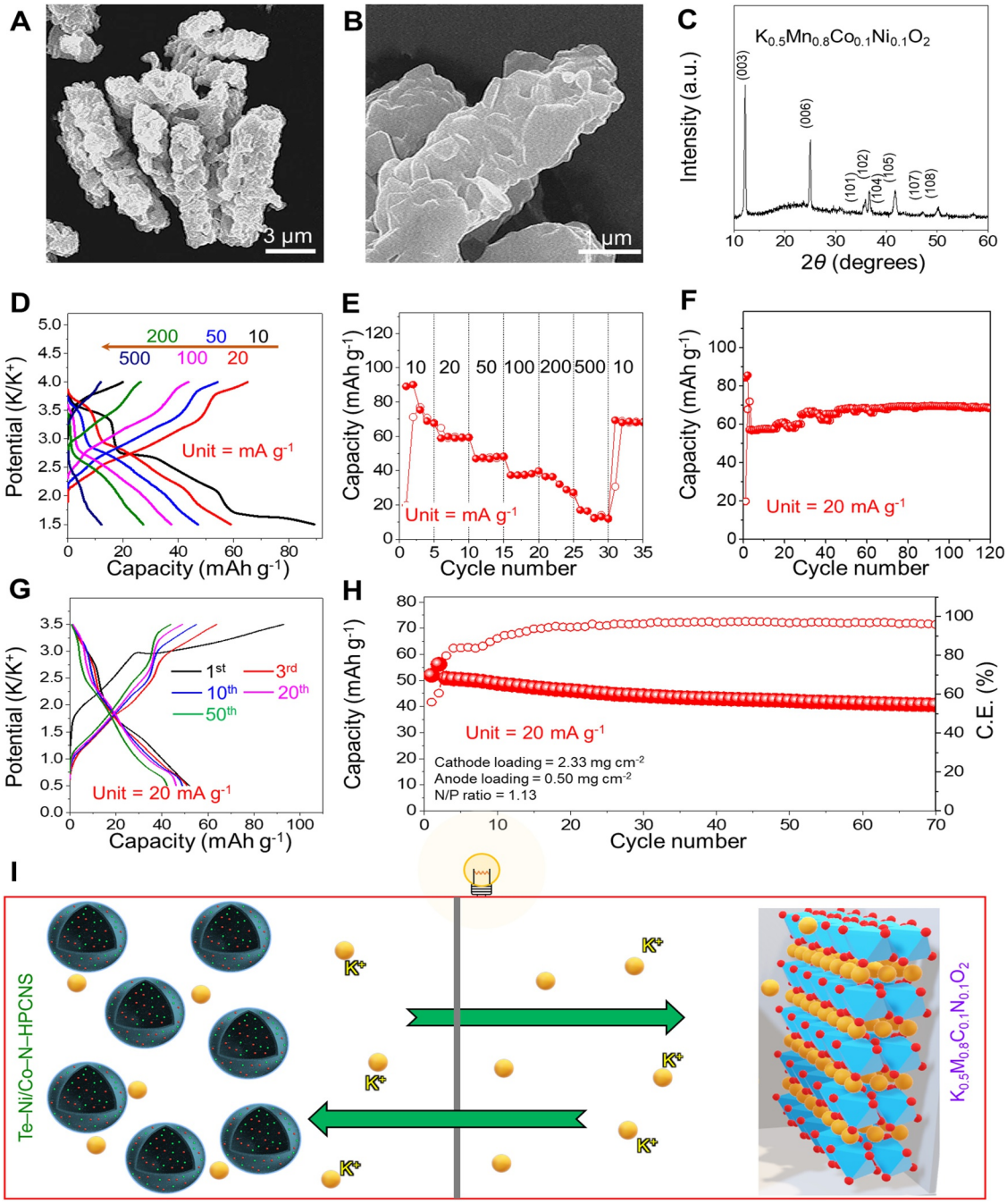

FIGURE 8 | Morphological and electrochemical investigations of half/full cells utilizing $K_{0.5}Mn_{0.8}Co_{0.1}Ni_{0.1}O_2$ (KMCNO) cathode. (A,B) FE–SEM micrographs of the KMCNO cathode; (C) XRD pattern; (D) galvanostatic charge-discharge voltage profiles across various current densities ranging from 10 to 500 mA g^{-1}; (E) rate capability tests; (F) cycling performance of the cathode half-cell at 20 mA g^{-1}; (G) galvanostatic charge-discharge curves for the full-cell at 20 mA g^{-1}; (H) cycling performance of the full-cell at 20 mA g^{-1}; (I) schematic representation of full cell featuring KMCNO||Te–Ni/Co–N–HPCNS assembly.

Figures S14C and S15C. For the (7 × 7) Ni@N_3G (001) surface, the d- and p-band center values for Ni, C, and N atoms are −5.187, −5.192, and −4.575 eV, respectively, compared to −0.753, −5.421, and −4.925 eV for the (7 × 7) Co@N_3G (001) surface. In contrast, the d- and p-band center values for Ni, Co, C, and N atoms on the (7 × 7) Ni/Co@N_3G (001) surface are −1.455, −1.598, −6.163, and −6.638 eV, respectively. This indicates that the d-band centers of Ni and Co are closer to the Fermi level than when Ni or Co is present individually, which plays a role in narrowing the band gap. Furthermore, the adsorption energies of the polytellurides, such as K_2Te and K_5Te_3, on the (7 × 7) Ni@N_3G (001) surface were −3.120 and −0.056 eV, respectively (Supporting Information S1: Figure S14D–F). These values differ from −2.861 and −0.072 eV on the (7 × 7) Co@N_3G (001) surface (Supporting Information S1: Figure S15D–F). In comparison, for the (7 × 7) Ni/Co@N_3G (001) surface, the computed adsorption energies were −4.111 and −1.913 eV, respectively, as depicted in Figure 7D–F. Notably, these stronger adsorption energies indicate stable interactions of polytellurides with the (7 × 7) Ni/Co@N_3G (001)

surface, effectively restricting the shuttling of dissolved polytellurides between the positive and negative electrodes. The (7 × 7) $NiCo@N_3G$ (001) DAC surface acts as an electron reservoir due to its excellent electrical conductivity, with a narrower band gap compared to SACs, enhancing the electrical conductivity of the electrode and potentially catalyzing the electrode reaction. These results collectively highlight the potential of the (7 × 7) $Ni/Co@N_3G$ (001) DAC surface in elucidating the intrinsic mechanism that restricts polytelluride shuttling and in designing efficient polytelluride reservoirs. To further explore the factors contributing to the exceptional redox chemistry of the Te–Ni/Co–N–HPCNS cathode, post-cycling analysis was performed. Morphological changes in the electrode cycled at a 2.0C-rate were examined. FE–SEM images (Figure 7G, H) confirm that the morphology is preserved even after ultra-long cycling. The diffraction peaks in XRD pattern (Figure 7I) are primarily indexed to the K_2Te_3 phase with minimal traces of amorphous Te, indicating that the electrochemical reactions within the cells are highly reversible, with Te as the starting material and K_2Te_3 as the charged product. TEM images presented in Figure 7J,K are consistent with the FE–SEM results. Additionally, the hollow structure is well-preserved, with crystals clearly visible on the surface (Figure 7K). The crystal lattice fringe shown in HR–TEM image (Figure 7L) corresponds to the (430) diffraction plane of the K_2Te_3 phase. The SAED pattern (Figure 7M) also reveals diffraction rings analogous to the K_2Te_3 phase even after 3000 cycles. Furthermore, the uniform distribution of C, N, Te, K, and S (due to the presence of fluorosulfonyl anion in the electrolyte) validates the structural integrity of the prepared nanostructure during repeated potassiation and depotassiation. Notably, the presence of Ni and Co as heteroatom double catalysts is also evident, confirming the excellent stability of the DAC within the carbon skeleton. Based on these observations, the meticulously designed *N*-doped hollow porous carbon nanosphere with Ni and Co heteroatomic sites effectively inhibits the dissolution and shuttle effects of K–pTe_n species. More importantly, the hollow structure provides ample buffer space for volume accommodation during the redox reaction and establishes abundant chemical anchoring sites and robust physical confinement, which are crucial for achieving ultra-stable potassium storage in Te–Ni/Co–N–HPCNS.

3.5 | Full Cell Analysis for K-Ion Battery

K-ion full-cells were designed as proof of concept by employing Te–Ni/Co–N–HPCNS (anode) and $K_{0.5}Mn_{0.8}Co_{0.1}Ni_{0.1}O_2$ (KMCNO) microcuboids (cathode). Figure 8 depicts the morphological and crystal structure features of the KMNCO cathode along with the electrochemical performance. FE–SEM images (Figure 8A,B) disclose a cuboid-type shape. Besides, XRD pattern (Figure 8C) exhibits well-defined peaks associated with a P3-type layered structure with a *hexagonal* lattice (*R*3*m*). The rate-capability test (Figure 8D,E) reveals an initial discharge capacity of 89, 58, 47, 37, 36, and 17 mAh g^{-1} at 10, 20, 50, 100, 200, and 500 mA g^{-1}, respectively. During cycling at 20 mA g^{-1} (Figure 8F), a capacity retention of approximately 81% was observed after 120 cycles. KMCNO‖Te–Ni/Co–N–HPCNS full-cell was then assembled, assimilating KMCNO cathode (2.33 mg cm^{-2}) and Te–Ni/Co–N–HPCNS anode (0.5 mg cm^{-2}). The third charge-discharge voltage profile (Figure 8G) shows that the cell displayed a capacity of 64/51 mAh g^{-1} at 20 mA g^{-1}. During cycling at 20 mA g^{-1} (Figure 8H), a capacity retention of ~78% (~41 mAh g^{-1}) was observed at the end of the 70th cycle, highlighting its robust energy-storage capabilities. It is imperative to note that the cathode was synthesized in-house, demanding further refinement to enhance the performance.

Overall, we have demonstrated a rational strategy for utilizing heteronuclear double atom catalysts confined within the shell of hollow porous carbon nanospheres as hosts for tellurium impregnation. This design strategy yielded unparalleled cycling stability, efficient polytelluride adsorption, effective volume accommodation, and improved redox reaction kinetics.

4 | Conclusions

In summary, tellurium impregnated hollow porous carbon nanospheres grafted with double-atom catalysts as heteronuclear sites (Te–Ni/Co–N–HPCNS) were synthesized and evaluated comprehensively for phase formation during redox processes and the dissolution mechanism of K-polytellurides (K–pTe_n) using XRD, TEM, and XPS techniques. This nanostructure design strategy resulted in a hollow cavity, a crucial feature for mitigating volume fluctuations and facilitating efficient electrolyte penetration, thereby ensuring effective electrode wetting. Moreover, the *N*-doping significantly improves the conductivity of the architecture. Correspondingly, the cell featuring Te–Ni/Co–N–HPCNS electrode exhibits improved redox kinetics and higher K-ion diffusion characteristics, leading to high rate capability (up to 2.0C) and ultra-high cycling performance at 0.5C (600 cycles), 1.0C (1800 cycles), and 2.0C (3000 cycles). Density functional theory calculations strongly suggest that the enhanced electrochemical performance is mainly due to the presence of Ni/Co–DAC as heteronuclear sites, which prevents the dissolution of K–pTe_n species and accelerates reaction kinetics to unprecedented levels. Even when employed as a negative electrode in a full-cell configuration for reversible K-ions insertion/de-insertion, the cell delivered reversible discharge capacity values up to 70 cycles at 20 mA g^{-1}, establishing its potential for commercial applications.

Author Contributions

Sung Woo Cho: conceptualization, data curation, resources, visualization, writing – original draft. **Kun Woo Baek:** conceptualization, data curation, investigation, validation, writing – original draft. **Thillai Govindaraja Senthamaraikannan:** investigation, methodology, writing – original draft. **Hyun Woo Kim:** investigation, methodology, writing – original draft. **Dong-Hee Lim:** conceptualization, investigation, project administration. **Jin-Sung Park:** investigation, validation, writing – original draft. **Rakesh Saroha:** conceptualization, investigation, project administration, supervision, writing – original draft, writing – review and editing. **Jung Sang Cho:** conceptualization, funding acquisition, investigation, project administration, supervision, writing – review and editing.

Acknowledgments

This study was financially supported by the National Research Foundation of Korea (NRF) funded by the Ministry of Science and ICT (Grant No. RS-2023-00217581), the Global-Learning & Academic research

institution for Master's·pH.D. students, and Postdocs (G-LAMP) Program of the National Research Foundation of Korea (NRF) grant funded by the Ministry of Education (Grant No. RS-2023-00285390), the Regional Innovation System & Education (RISE) program through the (Chungbuk Regional Innovation System & Education Center), funded by the Ministry of Education (MOE) and the (Chungcheongbuk-do), Republic of Korea (Grant No. 2025-RISE-11-014-03), and the Korea Institute of Energy Technology Evaluation and Planning (KETEP) and the Ministry of Trade, Industry & Energy (MOTIE) of the Republic of Korea (Grant No. RS-2024-00394769).

Conflicts of Interest

The authors declare no conflicts of interest.

Data Availability Statement

The data that support the findings of this study are available from the corresponding author upon reasonable request.

References

1. Y. Zhang, H. Zhu, D. J. Freschi, and J. Liu, "High-Performance Potassium-Tellurium Batteries Stabilized by Interface Engineering," *Small* 18, no. 15 (2022): 2200085, https://doi.org/10.1002/smll.202200085.

2. R. Saroha, J. S. Cho, and J. H. Ahn, "Synergetic Effects of Cation (K^+) and Anion (S^{2-})-Doping on the Structural Integrity of Li/Mn-Rich Layered Cathode Material With Considerable Cyclability and High-Rate Capability for Li-Ion Batteries," *Electrochimica Acta* 366 (2021): 137471, https://doi.org/10.1016/j.electacta.2020.137471.

3. L. J. Xu, X. J. Wang, G. Y. Tang, et al., "NiSe Nanoparticles Anchored on Hollow Carbon Nanofibers With Enhnaced Rate Capability and Prolonged Cycling Durability for Sodium-Ion Batteries," *Rare Metals* 44, no. 1 (2025): 185–194, https://doi.org/10.1007/s12598-024-02956-7.

4. J. Yu, D. K. Kim, H. G. Oh, S. K. Park, and Y. N. Yoo, "P Co-Doped 3D Porous Carbon With Self-Assembled Morphological Control via Template-Free Method for Potassium-Ion Battery Anodes," *Rare Metals* 43, no. 9 (2024): 4243–4252, https://doi.org/10.1007/s12598-024-02724-7.

5. P. Wu, Z. Mu, K. Qian, C. Guo, M. Li, and J. Li, "Biochar-Derived Hierarchical Porous Carbon as Tellurium Host for High-Performance Potassium-Tellurium Batteries," *Chemistry—A European Journal* 29, no. 69 (2023): e202302121, https://doi.org/10.1002/chem.202302121.

6. F. Wang, J. Li, J. Zhao, et al., "Single-Atom Electrocatalysts for Lithium Sulfur Batteries: Progress, Opportunities, and Challenges," *ACS Materials Letters* 2, no. 11 (2020): 1450–1463, https://doi.org/10.1021/acsmaterialslett.0c00396.

7. D. Yu, Q. Li, W. Zhang, and S. Huang, "Amorphous Tellurium-Embedded Hierarchical Porous Carbon Nanofibers as High-Rate and Long-Life Electrodes for Potassium-Ion Batteries," *Small* 18, no. 32 (2022): 2202750, https://doi.org/10.1002/smll.202202750.

8. X. Huang, J. Sun, L. Wang, X. Tong, S. X. Dou, and Z. M. Wang, "Advanced High-Performance Potassium–Chalcogen (S, Se, Te) Batteries," *Small* 17, no. 6 (2021): 2004369, https://doi.org/10.1002/smll.202004369.

9. X. L. Huang, Z. Guo, S. X. Dou, and Z. M. Wang, "Rechargeable Potassium–Selenium Batteries," *Advanced Functional Materials* 31, no. 29 (2021): 2102326, https://doi.org/10.1002/adfm.202102326.

10. J. Zhou, D. Shen, X. Yu, and B. Lu, "Building Ultra-Stable K–Te Battery by Molecular Regulation," *Journal of Energy Chemistry* 69 (2021): 100–107, https://doi.org/10.1016/j.jechem.2021.10.001.

11. S. Dong, D. Yu, J. Yang, et al., "Tellurium: A High-Volumetric-Capacity Potassium-Ion Battery Electrode Material," *Advanced Materials* 32, no. 23 (2020): 1908027, https://doi.org/10.1002/adma.201908027.

12. R. Saroha, J. H. Oh, Y. H. Seon, Y. C. Kang, J. S. Lee, and J. S. Cho, "Freestanding Interlayers for Li-S Batteries: Design and Synthesis of Hierarchically Porous *N*-Doped C Nanofibers Comprising Vanadium Nitride Quantum Dots and MOF-Derived Hollow *N*-Doped C Nanocages," *Journal of Materials Chemistry A* 9, no. 19 (2021): 11651–11664, https://doi.org/10.1039/DITA01802G.

13. H. Yuan, W. Zhang, J. G. Wang, et al., "Facilitation of Sulfur Evolution Reaction by Pyridinic Nitrogen Doped Carbon Nanoflakes for Highly-Stable Lithium-Sulfur Batteries," *Energy Storage Mater* 10 (2018): 1–9, https://doi.org/10.1016/j.ensm.2017.07.015.

14. R. Saroha, J. H. Oh, J. S. Lee, et al., "Hierarchically Porous Nanofibers Comprising Multiple Core–Shell Co_3O_4@graphitic Carbon Nanoparticles Grafted Within *N*-Doped CNTs as Functional Interlayers for Excellent Li–S Batteries," *Chemical Engineering Journal* 426 (2021): 130805, https://doi.org/10.1016/j.cej.2021.130805.

15. R. Saroha, J. H. Ahn, and J. S. Cho, "A Short Review on Dissolved Lithium Polysulfide Catholytes for Advanced Lithium-Sulfur Batteries," *Korean Journal of Chemical Engineering* 38, no. 3 (2021): 461–474, https://doi.org/10.1007/s11814-020-0729-5.

16. H. Xu and A. Manthiram, "Hollow Cobalt Sulfide Polyhedra-Enabled Long-Life, High Areal-Capacity Lithium-Sulfur Batteries," *Nano Energy* 33 (2017): 124–129, https://doi.org/10.1016/j.nanoen.2017.01.007.

17. R. Saroha and J. S. Cho, "Nanofibers Comprising Interconnected Chain-Like Hollow *N*-Doped C Nanocages as 3D Free-Standing Cathodes for Li–S Batteries With Super-High Sulfur Content and Lean Electrolyte/Sulfur Ratio," *Small Methods* 6, no. 5 (2022): 2200049, https://doi.org/10.1002/smtd.202200049.

18. R. Saroha, H. S. Ka, G. D. Park, C. Cho, D. W. Kang, and J. S. Cho, "Long-Term Stability of Lithium–Sulfur Batteries via Synergistic Integration of Nitrogen-Doped Graphitic Carbon-Coated Cobalt Selenide Nanocrystals Within Porous Three-Dimensional Graphene-Carbon Nanotube Microspheres," *Journal of Power Sources* 592 (2024): 233893, https://doi.org/10.1016/j.jpowsour.2023.233893.

19. Y. H. Seon, R. Saroha, and J. S. Cho, "Hierarchically Porous *N*-Doped C Nanofibers Comprising TiO_2 Quantum Dots and ZIF-8-Derived Hollow *C* Nanocages as Ultralight Interlayer for Stable Li–S Batteries," *Composites Part B: Engineering* 237 (2022): 109856, https://doi.org/10.1016/j.compositesb.2022.109856.

20. G. Liang, J. Wu, X. Qin, et al., "Ultrafine TiO_2 Decorated Carbon Nanofibers as Multifunctional Interlayer for High-Performance Lithium–Sulfur Battery," *ACS Applied Materials and Interfaces* 8, no. 35 (2016): 23105–23113, https://doi.org/10.1021/acami.6b07487.

21. R. Saroha, Y. H. Seon, B. Jin, et al., "Self-Supported Hierarchically Porous 3D Carbon Nanofiber Network Comprising Ni/Co/$NiCo_2O_4$ Nanocrystals and Hollow *N*-Doped C Nanocages as Sulfur Host for Highly Reversible Li–S Batteries," *Chemical Engineering Journal* 446 (2022): 137141, https://doi.org/10.1016/j.cej.2022.137141.

22. Y. J. Lei, H. L. Yang, Y. Liang, et al., "Progress and Prospects of Emerging Potassium–Sulfur Batteries," *Advanced Energy Materials* 12, no. 46 (2022): 2202523, https://doi.org/10.1002/aenm.202202523.

23. R. Saroha, H. S. Ka, and J. S. Cho, "A Novel Three-Dimensional Ordered Mesoporous Microspheres Comprising *N*-Doped Graphitic Carbon-Coated Fe_xP Nanoparticles as Multifunctional Interlayers to Suppress Polysulfide Crossover in Li–S Batteries," *Applied Surface Science* 612 (2022): 155892, https://doi.org/10.1016/j.apsusc.2022.155892.

24. S. Li, J. Warzywoda, S. Wang, G. Ren, and Z. Fan, "Bacterial Cellulose Derived Carbon Nanofiber Aerogel With Lithium Polysulfide Catholyte for Lithium–Sulfur Batteries," *Carbon* 124 (2017): 212–218, https://doi.org/10.1016/j.carbon.2017.08.062.

25. J. M. Choi, R. Saroha, J. S. Kim, M. R. Jang, and J. S. Cho, "Porous Nanofibers Comprising VN Nanodots and Densified *N*-Doped CNTs as

Redox-Active Interlayers for Li–S Batteries," *Journal of Power Sources* 59 (2023): 232632, https://doi.org/10.1016/j.jpowsour.2023.232632.

26. R. Saroha, H. H. Choi, and J. S. Cho, "Boosting Redox Kinetics Using Rationally Engineered Cathodic Interlayers Comprising Porous rGO–CNT Framework Microspheres With $NiSe_2$-Core@*N*-Doped Graphitic Carbon Shell Nanocrystals for Stable Li–S Batteries," *Chemical Engineering Journal* 473 (2023): 145391, https://doi.org/10.1016/j.cej.2023.145391.

27. D. Yu, W. Zhang, Q. Zhang, and S. Huang, "Tuning Anion Chemistry Enables High-Voltage and Stable Potassium-Based Tellurium-Graphite Batteries," *Nano Energy* 92 (2022): 106744, https://doi.org/10.1016/j.nanoen.2021.106744.

28. Q. Liu, W. Deng, and C. F. Sun, "A Potassium–Tellurium Battery," *Energy Storage Mater* 28 (2020): 10–16, https://doi.org/10.1016/j.ensm.2020.02.021.

29. S. H. Yang, J. M. Choi, R. Saroha, S. W. Cho, Y. C. Kang, and J. S. Cho, "Hollow Porous Carbon Nanospheres Containing Polar Cobalt Sulfide (Co_9S_8) Nanocrystals as Electrocatalytic Interlayers for the Reutilization of Polysulfide in Lithium–Sulfur Batteries," *Journal of Colloid and Interface Science* 645 (2023): 33–44, https://doi.org/10.1016/j.jcis.2023.04.083.

30. Y. Zhang, C. Liu, Z. Wu, et al., "Enhanced Potassium Storage Performance for K-Te Batteries via Electrode Design and Electrolyte Salt Chemistry," *ACS Applied Materials and Interfaces* 13, no. 14 (2021): 16345–16354, https://doi.org/10.1021/acsami.1c01155.

31. X. Wang, K. Qian, M. Zhou, M. Li, C. Guo, and J. Li, "Hierarchical Microspheres Constructed by Te@*N*-Doped Carbon for Efficient Potassium Storage," *European Journal of Inorganic Chemistry* 22 (2021): 2141–2147, https://doi.org/10.1002/ejic.202100157.

32. Z. Shi, L. Wang, H. Xu, et al., "A Soluble Single Atom Catalyst pr/Omotes Lithium Polysulfide Conversion in Lithium Sulfur Batteries," *Chemical Communications* 55, no. 80 (2019): 12056–12059, https://doi.org/10.1039/C9CC06168A.

33. D. Wang, K. Ma, J. Hao, et al., "Engineering Single-Atom Catalysts as Multifunctional Polysulfide and Lithium Regulators Toward Kinetically Accelerated and Durable Lithium-Sulfur Batteries," *Chemical Engineering Journal* 466 (2023): 143182, https://doi.org/10.1016/j.cej.2023.143182.

34. C. Xu, B. Ding, Z. Fan, et al., "Theoretical and Experimental Understanding of Metal Single-Atom Electrocatalysts for Accelerating the Electrochemical Reaction of Lithium–Sulfur Batteries," *ACS Applied Materials and Interfaces* 14, no. 34 (2022): 38750–38757, https://doi.org/10.1021/acsami.2c09430.

35. T. H. Tian, S. Wang, S. Chen, et al., "High-Power Lithium–Selenium Batteries Enabled by Atomic Cobalt Electrocatalyst in Hollow Carbon Cathode," *Nature Communications* 11, no. 1 (2020): 5025, https://doi.org/10.1038/s41467-020-18820-y.

36. H. Lin, Z. Guo, Q. Zhang, et al., "Coupled Ni-Co Dual-Atom Catalyst for Guiding Sulfur and Lithium Evolutions in Lithium–Sulfur Batteries," *Small* 20, no. 46 (2024): 2404983, https://doi.org/10.1002/smll.202404983.

37. J. S. Lee, M. S. Jo, R. Saroha, et al., "Hierarchically Well-Developed Porous Graphene Nanofibers Comprising *N*-Doped Graphitic *C*-Coated Cobalt Oxide Hollow Nanospheres as Anodes for High-Rate Li-Ion Batteries," *Small* 16, no. 32 (2020): 2002213, https://doi.org/10.1002/smll.202002213.

38. J. S. Lee, R. Saroha, S. H. Oh, et al., "Rational Design of Perforated Bimetallic (Ni, Mo) Sulfides/*N*-Doped Graphitic Carbon Composite Microspheres as Anode Materials for Superior Na-Ion Batteries," *Small Methods* 5, no. 9 (2021): 2100195, https://doi.org/10.1002/smtd.202100195.

39. C. S. Kim, J. S. Lee, R. Saroha, et al., "Porous Nitrogen-Doped Graphene Nanofibers Comprising Metal Organic framework-derived Hollow and Ultrafine Layered Double Metal Oxide Nanocrystals as High-Performance Anodes for Lithium-Ion Batteries," *Journal of Power Sources* 523 (2022): 231030, https://doi.org/10.1016/j.jpowsour.2022.231030.

40. J. Salmón-Gamboa, A. Barajas-Aguilar, L. Ruiz-Ortega, A. Garay-Tapia, and S. Jiménez-Sandoval, "Vibrational and Electrical Properties of $Cu_{2-x}Te$ Films: Experimental Data and First Principle Calculations," *Scientific Reports* 8, no. 1 (2018): 8093, https://doi.org/10.1038/s41598-018-26461-x.

41. N. Xu, P. Ma, S. Fu, et al., "Tellurene-Based Saturable Absorber to Demonstrate Large-Energy Dissipative Soliton and Noise-Like Pulse Generations," *Nanophotonics* 9, no. 9 (2020): 2783–2795, https://doi.org/10.13039/501100001809.

42. R. Saroha and A. K. Panwar, "Effect of In Situ Pyrolysis of Acetylene (C_2H_2) Gas as a Carbon Source on the Electrochemical Performance of $LiFePO_4$ for Rechargeable Lithium-Ion Batteries," *Journal of Physics D Applied Physics* 50, no. 25 (2017): 255501, https://doi.org/10.1088/1361-6463/aa708c.

43. J. S. Lee, R. Saroha, and J. S. Cho, "Porous Microspheres Comprising $CoSe_2$ Nanorods Coated With *N*-Doped Graphitic *C* and Polydopamine-Derived C as Anodes for Long-Lived Na-Ion Batteries," *Nano-Micro Letters* 14, no. 1 (2022): 1–22, https://doi.org/10.1007/s40820-022-00855-z.

44. J. S. Lee, R. Saroha, J. H. Oh, et al., "Camphene-Derived Hollow and Porous Nanofibers Decorated With Hollow NiO Nanospheres and Graphitic Carbon as Anodes for Efficient Lithium-Ion Storage," *Journal of Industrial and Engineering Chemistry* 114 (2022): 276–287, https://doi.org/10.1016/j.jiec.2022.07.017.

45. J. S. Lee, J. S. Park, K. W. Baek, et al., "Coral-Like Porous Microspheres Comprising Polydopamine-Derived *N*-Doped *C*-Coated $MoSe_2$ Nanosheets Composited With Graphitic Carbon as Anodes for High-Rate Sodium-and Potassium-Ion Batteries," *Chemical Engineering Journal* 456 (2022): 141118, https://doi.org/10.1016/j.cej.2022.141118.

46. J. S. Lee, H. S. Ka, R. Saroha, Y. C. Kang, D. W. Kang, and J. S. Cho, "Three-Dimensional Hierarchically Porous Micro Sponge-Ball Comprising Anatase TiO_2 Nanodots and Nitrogen-Doped Graphitic Carbon as Anodes for Ultra-Stable Lithium-Ion Batteries," *Journal of Energy Storage* 66 (2023): 107396, https://doi.org/10.1016/j.est.2023.107396.

47. R. Saroha, D. Y. Shin, J. S. Lee, S. W. Cho, D. H. Lim, and J. S. Cho, "Theoretically Endured Defect-Engineered Antimony Selenide Nanocrystals Grafted Within Three-Dimensional Reduced Graphene Oxide Hollow Microspheres With Large Open Cavities as Polysulfide Barrier for Robust Sulfur Kinetics," *Advanced Composites and Hybrid Material* 7, no. 3 (2024): 1–19, https://doi.org/10.1007/s42114-024-00892-9.

48. C. S. Kim, R. Saroha, and J. S. Cho, "*N*-Doped Graphene Nanofibers With Porous Channel Comprising FeS Nanocrystals and Intertwined *N*-Doped CNTs as Efficient Interlayers for Li-S Batteries," *International Journal of Energy Research*, no. 1 (2023): 3610577, https://doi.org/10.1155/2023/3610577.

49. P. Xiong, X. Han, X. Zhao, et al., "Room-Temperature Potassium–Sulfur Batteries Enabled by Microporous Carbon Stabilized Small-Molecule Sulfur Cathodes," *ACS Nano* 13, no. 2 (2019): 2536–2543, https://doi.org/10.1021/acsnano.8b09503.

50. Y. Yao, M. Chen, R. Xu, et al., "CNT Interwoven Nitrogen and Oxygen Dual-Doped Porous Carbon Nanosheets as Free-Standing Electrodes for High-Performance Na-Se and K-Se Flexible Batteries," *Advanced Materials* 30, no. 49 (2018): 1805234, https://doi.org/10.1002/adma.201805234.

51. Q. Li, D. Yu, J. Peng, et al., "Efficient Polytelluride Anchoring for Ultralong-Life Potassium Storage: Combined Physical Barrier and Chemisorption in Nanogrid-in-Nanofiber," *Nano-Micro Letters* 16, no. 1 (2024): 77, https://doi.org/10.1007/s40820-023-01318-9.

52. S. Tari, F. Aqariden, Y. Chang, C. Grein, J. Li, and N. Kioussis, "Impact of Surface Treatment on the Structural and Electronic Properties of Polished CdZnTe Surfaces for Radiation Detectors," *Journal of Electronic Materials* 42, no. 11 (2013): 3252–3258, https://doi.org/10.1007/s11664-013-2649-1.

53. T. Wei, J. Wei, K. Zhang, and L. Zhang, "Image Lithography in Telluride Suboxide Thin Film Through Controlling 'Virtual' Bandgap," *Photonics Research* 5, no. 1 (2017): 22–26, https://doi.org/10.1364/PRJ.5.000022.

Supporting Information

Additional supporting information can be found online in the Supporting Information section.
Supporting Information S1: rar270186-sup-0001-suppl-data.docx.